785-nm Frequency Comb-Based Time-of-Flight Detection for 3D Surface Profilometry of Silicon Devices

Hyunsoo Kwak, Changmin Ahn, Yongjin Na, Jinho Bae, and Jungwon Kim, *Senior Member, IEEE*

***Abstract*—Three-dimensional integrated circuits (3D-ICs) are becoming more significant in portable devices, autonomous vehicles, and data centers. As the demand for highly integrated and high-performance semiconductor devices grows, recent 3D integration technologies focus on lowering the size of the micro-structures on such devices for high density. In order to inspect the 3D semiconductor devices, it is critical to measure the heights, depths, and overall surface profiles of the micro-structures made with silicon materials. Here, we demonstrate precise surface imaging for silicon devices by using a femtosecond mode-locked laser centered at 785 nm wavelength and an electro-optic sampling-based time-of-flight detection method with sub-10-nanometer axial precision. We could successfully measure the surface profiles as well as the step heights of silicon wafer stacks and micro-scale structures on silicon substrates.**

***Index Terms*—Electro-optic sampling, frequency comb, semiconductor device metrology, surface profilometry.**

I. Introduction

WITH the recent explosive demands for highly integrated and multifunctional semiconductor devices, three-dimensional (3D) semiconductor integration technology has been remarkably developed [1], [2]. To achieve high functionality as a single device, multiple integrated circuits (ICs), such as processors, memory chips and image sensors, are stacked vertically on a single die [3]. Recently, for high device density, the size of micro-scale structures on ICs such as micro-bumps [4], [5] or through-silicon vias (TSVs) [6] are reduced to <10 μm. As 3D-ICs have more complex structures and smaller device sizes, accurate and precise surface imaging becomes critical to prevent device failures [7], [8], [9], [10].

Previously, in semiconductor device fabrication facilities, to measure the surface profile of the semiconductor devices, various approaches have been used [11], [12]. Table I summarizes the comparison of representative surface profilometry methods for semiconductor devices. Electron microscopy [13], [14], [15] has the advantage of high spatial resolution of <0.1 nm; however, to obtain high-resolution images, field-of-view (FOV) is sacrificed to several tens to hundreds of nanometers, resulting in a long time for fully imaging the wafer-level surface. In addition, one of the main limitations of electron microscopy is that it can cause beam damage to the sample. Atomic force microscopy [16] has a high vertical resolution of <0.01 nm, but its slow scan rate is not suitable for the high-speed measurements required in integrated circuit production. The interferometry-based surface metrology [17], [18], [19], [20] has the advantage of sub-nanometer resolution; however, its narrow ambiguity range of sub-micrometer makes it difficult to obtain surface profiles of wafer-level thicknesses. Confocal microscopy [21] is commonly used for surface imaging of step structures with hundreds of nanometer axial resolutions. However, since the axial resolution of confocal microscopy is limited by diffraction, it requires a large numerical aperture of the objective lens for high axial resolution at the expense of FOV. Therefore, confocal microscopy generally takes a long time to obtain high-resolution surface images. Optical frequency comb-based surface imaging has also been demonstrated, such as dual-comb interferometry [22]. Dual-comb interferometry has a large measurable range of several meters, but in order to achieve high-precision, the measurement speed should be sacrificed because it is determined by the detune frequency between the two frequency combs. As a result, to obtain high-resolution surface images, existing methods sacrifice either measurement speed, precision, or measurable ranges. However, 3D-IC production processes still require fast and precise surface metrology with a large measurable range of wafer-level thicknesses.

Recently, a new time-of-flight (TOF)-based surface imaging method using an electro-optic sampling-based timing detection (EOS-TD) with erbium-doped fiber frequency comb was reported [23], [24]. The strength of this approach is a unique combination of ultrafast measurement speed and sub-nanometer precision over the measurable range of several millimeters. When using a Galvano scanner, this TOF detection method allowed for precise surface imaging of metallic surfaces such as gold, steel, and chromium. However, a 1560-nm femtosecond laser pulse penetrates semiconductor materials such as silicon (Si), which is commonly used as a substrate for semiconductor devices, causing multiple reflections at the surface. Accurate

Manuscript received 17 June 2022; revised 20 August 2022; accepted 30 August 2022. Date of publication 5 September 2022; date of current version 14 September 2022. This work was supported by the National Research Foundation of Korea under Grant NRF-2021R1A5A1032937. *(Corresponding author: Jungwon Kim.)*

The authors are with the Korea Advanced Institute of Science and Technology, Daejeon 34141, Republic of Korea (e-mail: sukus1041@kaist.ac.kr; chang9592@kaist.ac.kr; terry762@kaist.ac.kr; jinho6536@kaist.ac.kr; jungwon.kim@kaist.ac.kr).

Digital Object Identifier 10.1109/JPHOT.2022.3203988

This work is licensed under a Creative Commons Attribution 4.0 License. For more information, see https://creativecommons.org/licenses/by/4.0/

TABLE I
PERFORMANCE COMPARISON OF SURFACE PROFILOMETRY OF SEMICONDUCTOR DEVICES

	Electron microscopy [13]-[15]	Atomic force microscopy [16]	Interferometry [17]-[20]	Confocal microscopy [21]
Acquisition time	1-10 sec.	1-10 sec.	0.01-1 sec.	0.1-1 sec.
Lateral resolution	<1 nm for SEM <0.1 nm for TEM	1-10 nm	10-100 μm (depending on imaging system)	200-500 nm (diffraction limit)
Vertical resolution	--	<0.01 nm	0.1-10 nm	200-500 nm (diffraction limit)
Field-of-view	10-100 nm (for high resolution)	Tens of nanometers (depending on scanner)	Several millimeters (depending on imaging system)	A few millimeters (depending on imaging system)
Disadvantages	Beam damage	Slow scan rate	Sub-μm ambiguity range	Slow scan rate

TOF detection at the silicon surface is difficult because TOF signals transmitted through the silicon substrate and reflected from the bottom surface multiple times are detected together by a single detector. Therefore, Si-based micro-structure imaging with a 1560-nm laser source has not been possible with this TOF detection method.

In this study, we extend this electro-optic sampling-based TOF approach to shorter wavelength ranges by utilizing the 785-nm femtosecond laser pulses by frequency-doubling the mode-locked Er-fiber laser centered at 1570 nm. We could show that a fast and precise step height measurement and surface profilometry for the structures on a Si surface is possible using 785-nm femtosecond laser pulses. Femtosecond pulses at 785 nm are suitable for surface imaging of Si-based semiconductor devices due to its low penetration depth of $\sim$8 μm in silicon, which is $\delta = \lambda/(4\pi \cdot \mathrm{Im}[n]) = 8.06\ \mu$m, where δ is the penetration depth, λ is the wavelength, and n is the complex refractive index. Since silicon wafers used in 3D-ICs fabrication commonly have a thickness of several hundred micrometers, 785-nm light transmitted through the silicon substrate is almost absorbed. By exploiting these properties, we employed an EOS-TD made with fiber optic components operating at an 800-nm wavelength range for rapid and precise Si surface imaging. As a result, our method enables TOF detection with high speed (up to 20 MHz update rate), high precision (down to 4 nm), and a large measurable range (up to 9.3 mm). Further, we demonstrated the step height and surface profile measurement of Si-based samples by using the TOF detection when scanning the sample with motorized stages or a Galvano scanner.

II. OPERATION PRINCIPLES AND EXPERIMENTAL SETUP

Fig. 1 shows the operation principle and experimental setup. The experimental setup is placed in a polycarbonate shielding box to reduce air and temperature fluctuations. In order to generate optical pulses in the shorter wavelength (close to visible wavelength range), where the penetration depth is low in Si materials, in a simple, low-cost and robust way, second-harmonic generation (SHG) of a femtosecond mode-locked Er-fiber laser output is employed. In this work, a 79.2-MHz optical pulse train with a $\sim$785 nm center wavelength (see Fig. 1(a)) and $\sim$85-fs pulsewidth (FemtoFiber smart 780, Toptica) is used. After $\sim$80 mW optical pulse train emitted from the laser is coupled into a polarization maintaining (PM) optical fiber ($\sim$56 mW), the pulse train is split into two paths by a 70:30 coupler: the reference arm (30%) is used for timing synchronization between femtosecond optical pulses and the microwave oscillator, and the measurement arm (70%) is used for detecting the TOF changes in optical pulses. By focusing the beam on the step structures and scanning it by motorized stages or a Galvano scanner, the TOF of the reflected pulse changes according to the step height of the structures. When optical power of $\sim$35 mW is incident on the Si surface through the collimator-lens array, due to the $\sim$30% reflectivity of the Si material at 785 nm, the resulting returned optical power of the reflected light (including the loss at the collimator) is $\sim$6 mW. In this work, we focused on measuring flat surfaces. Theoretically, in specular reflection, the maximum allowable surface slope that can collect returned optical power from the sample surface is determined by the numerical aperture (NA) of the objective lens as $\alpha_{\max} = \sin^{-1}$(NA). Since our imaging system has $\alpha_{\max}$ of $<3^\circ$, careful alignment is required to reduce the decrease in collected optical power due to the surface slope in the sample.

In order to generate the frequency-locked electronic signal as well as to detect the TOF changes, two EOS-TDs are employed. Among several EOS-TD configurations [25], [26], [27], [28], we used the all-PM-fiber Sagnac-loop interferometer configuration, which was also previously employed for long-term sub-10-fs synchronization between an 800-nm Ti:sapphire laser and a microwave oscillator for ultrafast electron diffraction (UED) facilities [29], [30], [31]. The reference arm and the EOS-TD 1 (in Fig. 1) are constructed to provide a reference timing ruler signal to the TOF-detecting EOS-TD (EOS-TD 2 in Fig. 1) as

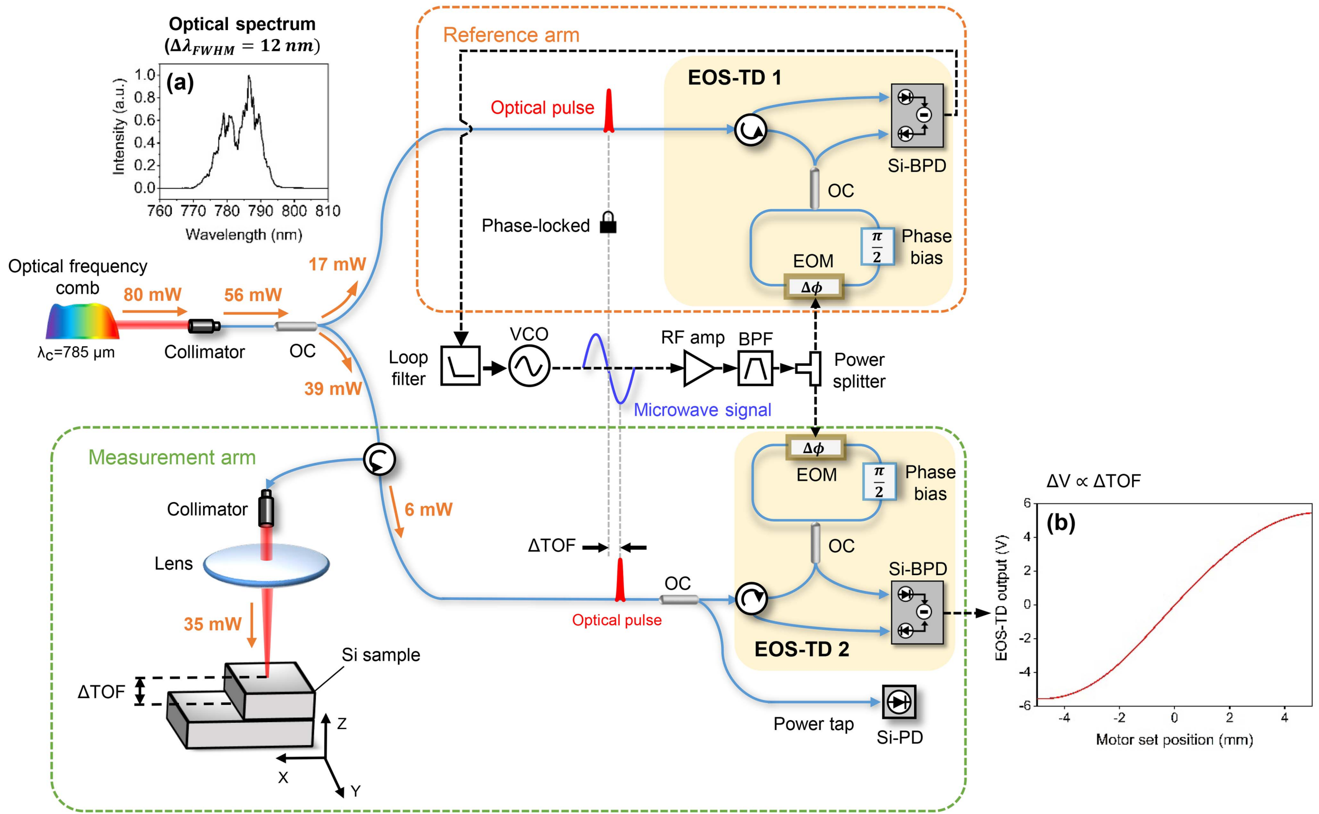

Fig. 1. Operation principle and experimental setup. Schematic of the EOS-TD-based TOF detection method using a 785 nm optical frequency comb source. OC, optical coupler; Si-PD, silicon photodiode; Si-BPD, silicon balanced photodetector; EOM, electro-optic phase modulator; VCO, voltage-controlled oscillator; RF amp, RF amplifier; BPF, microwave bandpass filter. (a) Measured optical spectrum shows ∼12 nm full-width-at-half-maximum (FWHM) bandwidth. (b) EOS-TD output response according to motor set position.

a phase-locked microwave signal generated from an 8-GHz microwave voltage-controlled oscillator (VCO). Note that the VCO frequency should be matched to multiples of the optical pulse repetition rate ($N\ f_{rep} = 102 \times 79.2\ MHz = 8.07\ GHz$ is used in this work). When an optical pulse train is applied to the EOS-TD, the optical phase in the optical pulse is modulated by a unidirectional electro-optic phase modulator (EOM) driven by the microwave signal generated from the VCO. A non-reciprocal $\pi/2$-phase bias unit is employed for the intensity balancing of the two outputs from the EOS-TD. As a result, the relative timing difference between counter-propagating pulses in the Sagnac loop is proportional to the intensity difference between the two outputs from the Sagnac loop. By measuring the difference in two outputs of the EOS-TD with a Si balanced photodetector (BPD), the timing difference between the optical pulse positions and the zero-crossing positions of the VCO microwave signal can be obtained. The insertion losses of the EOM, circulator, and phase bias unit in the EOS-TD are 5 dB, 1.8 dB, and 1.2 dB, respectively, and the resulting power efficiency of the 785-nm EOS-TD is ∼4–5%. As a result, in the balanced condition, ∼670 μW of optical power is applied to each photodiode of the Si-BPD in the reference arm. For the construction of the phase-locked loop, a loop filter (LB-1005, Newfocus) and an 8-GHz VCO (HMC-C200, Hittite) are used. To maximize the detection sensitivity of the EOS-TD, the microwave signal from the VCO is amplified with a radio-frequency (RF) amplifier (NBL00437, Nextec-RF). The harmonic frequency components of the VCO are suppressed [26] by using an RF bandpass filter (6C52-8000/T200-O/O).

The optical pulse train reflected from the step structures, which experience the TOF changes according to the step height difference, is applied to the EOS-TD in the measurement arm (EOS-TD 2 in Fig. 1). Since the EOS-TD phase modulates optical pulses by the EOM driven by timing-synchronized microwave signal generated from the reference arm (EOS-TD 1 in Fig. 1), the TOF changes induced by the step structures are precisely detected as the voltage changes at the Si-BPD output of the EOS-TD 2. In this way, the height profile of the step structure can be reconstructed. Note that, to calibrate the power variations from the focusing position of the step structures, the power of the reflected light is also directly detected by a Si-photodetector (Si-PD).

Note that a look-up table is used to calibrate the nonlinearity of EOS-TD response in the full measurable range. As can be seen in Fig. 1(b), the EOS-TD output shows a sinusoidal waveform because the microwave generated from the VCO is a single-tone sinusoidal wave of ∼8 GHz. Since the electric waveforms generated by VCO are nonlinear at both ends, nonlinearity calibration is required for linear TOF detection over the entire measurable range. We made a look-up table by measuring the EOS-TD

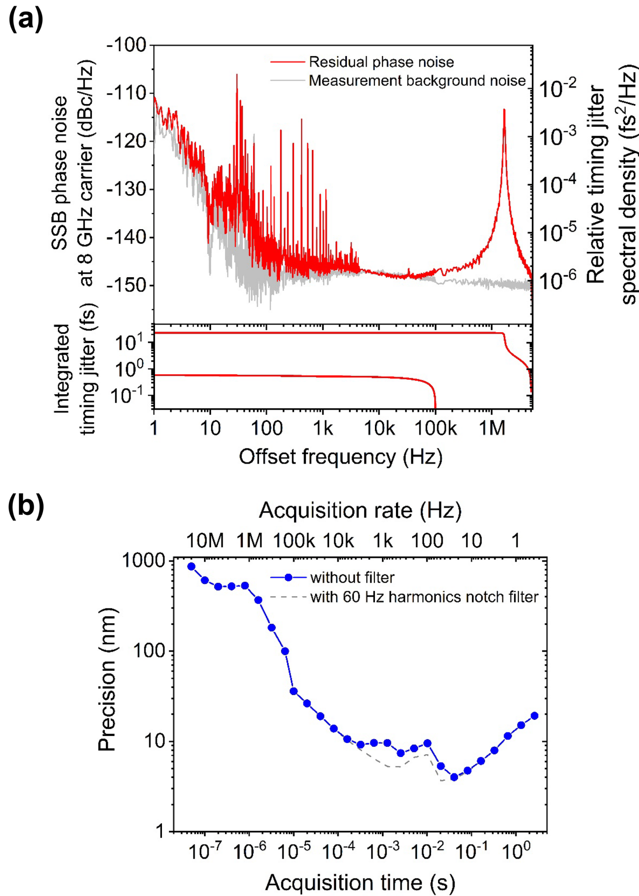

Fig. 2. Phase noise spectra and axial precision analysis. (a) Single-side band (SSB) residual phase noise spectra at 8 GHz carrier frequency (left) and the equivalent relative timing jitter PSDs (right). The integrated root-mean-square (r.m.s.) timing jitter from 1 Hz to 5 MHz is plotted on the bottom panel. (b) Measured TOF precision as a function of acquisition time. We evaluated measurement precision by calculating overlapping Allan deviation. The grey dashed line denotes the precision result with 60-Hz harmonics notch filters (at 60, 120, 180, 240, 300 Hz).

response according to the motor position with a precision motor stage (M-404.2DG, PI) by axially scanning a flat silver mirror as a target.

III. Evaluation of Axial Precision in the Time-of-Flight Detection

To evaluate the residual phase noise of the EOS-TD in the measurement arm (EOS-TD 2 in Fig. 1), we measured the voltage noise power spectra with a fast Fourier transform (FFT) spectrum analyzer (SR760, Stanford Research Systems) in the offset frequency range of 1 Hz - 100 kHz. For the offset frequency range of 100 kHz – 5 MHz, voltage noise spectra were measured with an RF spectrum analyzer (E4440A, Keysight). Fig. 2(a) shows the timing and phase noise power spectral densities (PSDs). Note that the measurement was performed without the sensor head and the output of the EOS-TD was placed at the zero-crossing of the VCO signals to maximize the detection sensitivity by using a motorized delay line (ODL-650, Oz-optics). The minimum residual phase noise floor reaches -148 dBc/Hz with an integrated root-mean-square (r.m.s.) timing jitter of 0.58 fs in the offset frequency range of 1 Hz–100 kHz and 23.55 fs in the offset frequency range of 1 Hz–5 MHz. In this experiment, the EOS-TD measurement background noise in the reference arm determines the minimum noise floor, where it is measured when optical pulses are applied to the Sagnac-loop without microwave signals.

To evaluate the axial precision performance in TOF detection, overlapping Allan deviation is calculated as shown in Fig. 2(b). The fastest acquisition rate is determined by the laser repetition rate of 79.2 MHz, but in this work, we could evaluate the precision up to 20 MHz acquisition rate due to the bandwidth of the used balanced photodetector. At 50-ns acquisition time, the precision is measured to be 867 nm. As shown in Fig. 2(a), since the resonance peak in the phase-locked loop (PLL) exists at ∼1.6 MHz, the precision performance is degraded at acquisition rates from 100 kHz to 5 MHz. At 10-μs acquisition time, the precision is measured to be 36 nm. As the acquisition time increases, the precision performance is improved to 4 nm at 40-ms acquisition time due to the averaging effect. After 40-ms acquisition time, precision performance deteriorates due to the timing drift in the synchronization between optical pulses and microwaves in the EOS-TD. The non-ambiguity range (NAR) is determined to be ∼9.3 mm. As can be seen from the PSDs in Fig. 2(a), 60-Hz harmonics induced by power supplies deteriorate the precision performance at acquisition times from 0.2 ms to 40 ms. To evaluate the precision performance when power supply noises are suppressed, we applied digital notch filters with 60-Hz harmonic frequencies (integer multiples from 60 Hz to 300 Hz), which shows that the precision from 0.2 ms to 40 ms acquisition time is reduced to <7 nm (gray dashed line in Fig. 2(b)).

IV. Step Height and Surface Profile Measurements of Silicon-Based Samples

To demonstrate the step height measurement of the Si surface, a double-side polished Si wafer with a thickness of ∼777 μm was prepared. Fig. 3 shows the 3D surface imaging result of the Si wafer stack with ∼777 μm step height. A collimated beam of ∼1 mm diameter passes through an achromatic lens with a focal length of 150 mm and is focused on the Si surface with a measured beam size of ∼249 μm ($1/e^2$). By using x-y motorized stages (V-408, PI and MT1-Z8, Thorlabs) for sample scanning, the step height is measured to be 777.68 μm with repeatability (1-σ) of 51.3 nm for 25 consecutive measurements over 62 seconds (Fig. 3(a)). The reason why the repeatability performance is worse than the Allan deviation precision is that it is affected by the timing drift during the 62 seconds measurement time and the decrease in detection sensitivity due to the low reflectance (∼30%) at the Si surface. The surface of the Si wafer with 5 mm × 5 mm size is imaged by 100 × 100 pixels with a step size of 50 μm. At each measurement point on the Si wafer, the exposure time for TOF data measurement was 40 ms. The required time to measure 100 × 100 pixels is 400 seconds, but the actual measurement time was ∼80 minutes because it is limited by the motor scan speed (20 mm/s) and the motor settling time (∼0.5 seconds for each measurement point). In

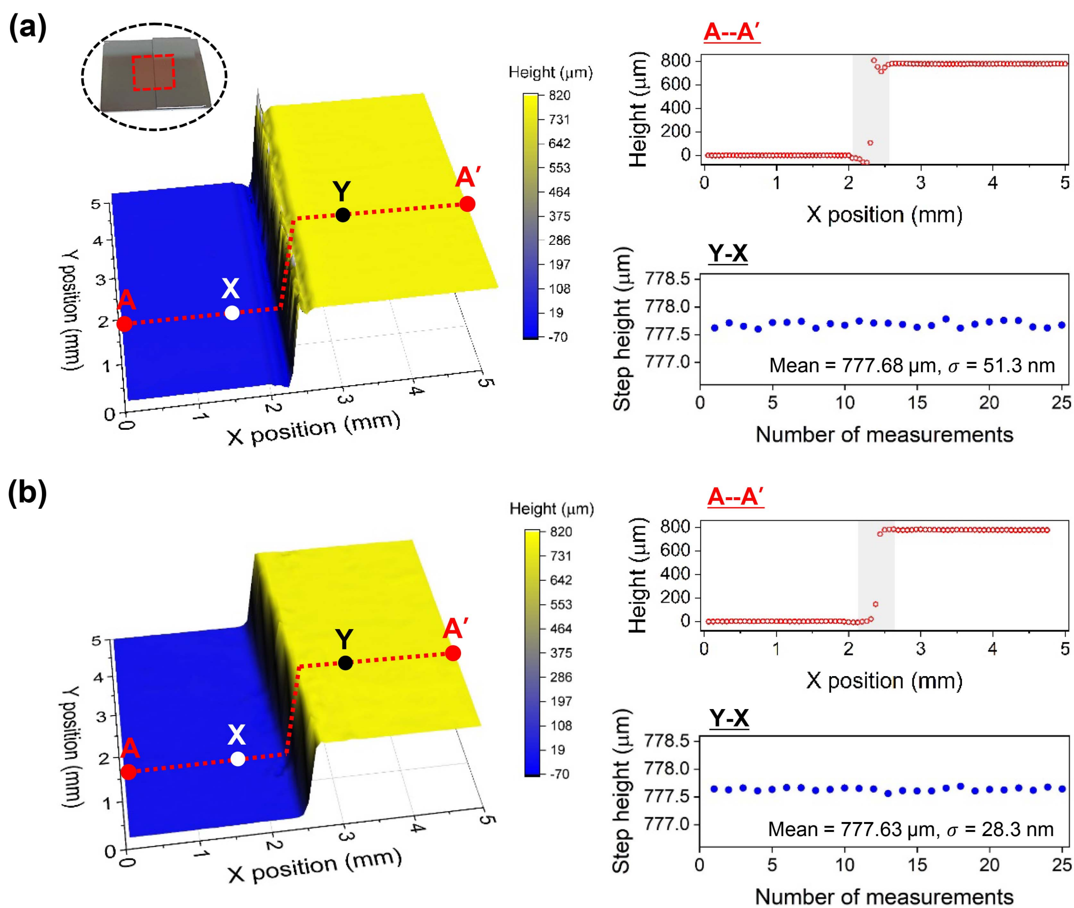

Fig. 3. Surface imaging results of silicon wafer stack. 3D surface image of Si wafer stack scanned by (a) a motorized linear stage and (b) a Galvano scanner. The mean step height between two surfaces (Y-X) is measured to be 777.68 μm and 777.63 μm, with 51.3 nm and 28.3 nm repeatability for (a) and (b), respectively. Note that the grey region indicates the edges between the two silicon wafers where the measured TOF has ambiguity due to reflections from two surfaces. The size of the grey region is determined by considering the measured beam size.

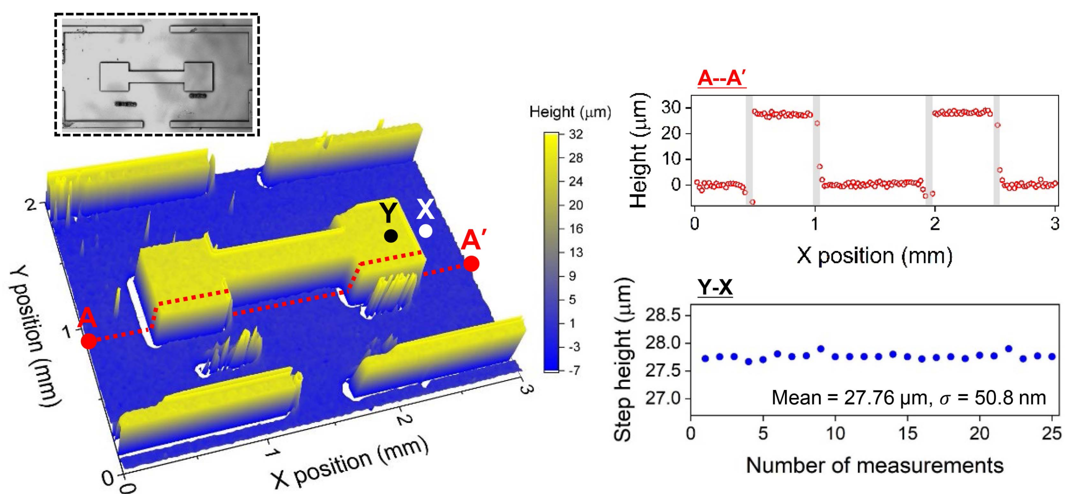

Fig. 4. Surface imaging results of silicon step-structures. 3D surface image reconstructed by TOF measurement of silicon step structures. The mean step height between two surfaces (Y-X) is measured to be 27.76 μm with 50.8 nm repeatability. Black dashed box shows the microscopic image of the silicon step structures. Note that the grey region indicates the edges between the bottom and top surfaces. The size of the grey region is determined by considering the measured beam size.

TABLE II
UNCERTAINTY EVALUATION OF THE OVERALL MEASUREMENT SYSTEM

Sources of uncertainty errors	Value	Value (nm) for L_0=150 mm and L_1=777 μm
① Systematic uncertainty of the EOS-TD	① = $\sqrt{②^2}$	15.5
② Uncertainty of sensitivity determination	② = $\sqrt{③^2 + ④^2}$	
③ Uncertainty of motor movement	$2 \times 10^{-5} \cdot L_1$	
④ Uncertainty of data acquisition board	0.6 μV ≈ 0.6 nm	
⑤ Statistical uncertainty for taking two TOF measurements with 0.5-ms acquisition time each	⑤ = $\sqrt{⑥^2}$	13.6
⑥ Uncertainty of relative timing between optical and microwave signals	13.6 nm	
ⓐ Combined uncertainty for TOF detection	ⓐ = $\sqrt{①^2 + ⑤^2}$	20.6
⑦ Uncertainty of beam scanning of a flat mirror with the Galvano scanner	⑦ = $\sqrt{⑧^2 + ⑨^2 + ⑩^2}$	61.5
⑧ Uncertainty of calibration mirror flatness	14.9 nm	14.9
⑨ Uncertainty related to the refractive index of air	$1.4 \times 10^{-7} \cdot L_0$	21
⑩ Uncertainty of beam scanning system	55.8 nm	55.8
ⓑ Combined uncertainty for TOF 3D imaging	ⓑ = $\sqrt{ⓐ^2 + ⑦^2}$	64.9
⑪ Uncertainty of flatness of silicon wafer	66.5 nm	66.5
⑫ Uncertainty related to the thermal expansion of silicon wafer	$5.7 \times 10^{-8} \cdot L_1$ (21 mK)	0.042
ⓒ Combined uncertainty	ⓒ = $\sqrt{ⓑ^2 + ⑪^2 + ⑫^2}$	92.9

*L_0 denotes the distance from the fiber collimator to the sample and L_1 denotes the step height of the Si wafer stack.

order to increase the measurement speed, the beam scanning speed was improved by using a Galvano x-y scanner (8310K, Cambridge Technology Inc.). Fig. 3(b) shows the 3D surface image of the silicon wafer stack by using a Galvano scanner. The repeatability improves down to 28.3 nm because the total measurement time (<1 second for 25 consecutive measures) is greatly reduced. Each measurement point was measured with 0.5 ms exposure time. The pixel size is ∼62 × 62 μm (separation between each measurement point), and the FOV is ∼5 × 5 mm. It takes <17 seconds to measure the 76 × 76 pixels. Note that the total imaging time is limited by the communication delay of the software used, and the actual total exposure time is 2.9 s. We expect that high-speed beam scanning devices such as acousto-optic deflectors will further improve the surface profile measurement speed.

A dog-bone-shaped Si step structure (SHS, AppNano) with a ∼28 μm height was prepared to show the step height measurement of the micro-scale Si structures. To measure Si step structures with a height of ∼28 μm, the beam size is reduced to ∼18.6 μm (1/e^2) using a ∼7.5 mm large beam collimator and an achromatic lens with a 75 mm focal length. Fig. 4 shows the surface imaging results of the dog-bone-shaped Si sample with a motorized stage. The step height is measured to be 27.76 μm with the repeatability (1-σ) of 50.8 nm for 25 consecutive measurements over 62 seconds.

We also evaluated the lateral resolution of our imaging system by measuring the resolution test target (USAF-1951). For each optical system used in Figs. 3 and 4, Element 2 in Group 2 and Element 3 in Group 5 are resolved well with a contrast of ∼37% and ∼30%, respectively. Therefore, the lateral resolution is determined to be 4.49 lp/mm (111.36 μm) and 40.3 lp/mm (12.4 μm), respectively.

In order to assess the accuracy of the method, we also compared the measured step height results with the results of confocal microscopy (LSM 980, Zeiss). Using the confocal microscopy, the mean step height of Si wafer stack and Si step

structures were measured to be 777.62 μm and 27.79 μm, at axial scan intervals of 200 nm and 100 nm, which shows +60 nm and -30 nm errors from the demonstrated TOF method, respectively. Since the root-mean-square flatness error of the double-side polished Si wafer stack is 66.5 nm [32], these errors are within the flatness of the Si wafer.

V. Evaluation of the Uncertainty Sources

We evaluated the uncertainty related to our 3-D imaging system (Table II). The uncertainty that can affect our system is (a) the uncertainty related to taking single-point TOF detection, (b) the uncertainty related to the 3D imaging system, and (c) the uncertainty related to the silicon wafer.

The major systematic uncertainty of the EOS-TD comes from the timing detection slope calibration. The accuracy and resolution of the precision motor stage can affect the uncertainty of the EOS-TD slope calibration (uncertainty of time grid; Line 3 in Table II). The uncertainty in slope calibration is $2 \times 10^{-5} \cdot L_1$ ($L_1$is the step height of the silicon wafer stack). The uncertainty from the voltage reading of the EOS-TD output is determined by the resolution of the data logger. The uncertainty from the data acquisition board (uncertainty of voltage grid; Line 4) is 0.6 nm (0.6 μV≈0.6 nm).

The repeatability (random error) for 0.5 ms averaging time was measured to be 9.6 nm as shown in Fig. 2(b). Since we need two TOF measurements to measure the step height, the random error is multiplied by $\sqrt{2}$, resulting in 13.6 nm uncertainty (Line 6). Therefore, the combined uncertainty of single-point TOF detection is evaluated to be 20.6 nm (Line a).

In the case of 3-D imaging, the uncertainty from the Galvano scanner for beam scanning should be considered. We measured the flat mirror to evaluate the uncertainty related to the beam scanning system. The measured uncertainty of the beam scanning of the flat mirror with the Galvano scanner was 61.5 nm (Line 7). This includes the uncertainty of the beam scanning itself (such as the wavefront error of a lens or beam alignment error), the flatness of a flat mirror, and the uncertainty related to the refractive index of air. The specified flatness of the flat mirror is given as 14.9 nm (Line 8). The uncertainty related to the refractive index of air (Line 9) is given by $1.4 \times 10^{-7} \cdot L_0 = 21$ nm (where L_0 is the distance from the fiber collimator to the sample when using the f = 150 mm lens; coefficient estimated from [33]). Therefore, the uncertainty related to beam scanning itself is evaluated as 55.8 nm (Line 10). The total amount of uncertainty during 3-D imaging using a Galvano scanner with an averaging time of 0.5 ms is 64.9 nm (Line b).

The flatness (root-mean-square) of the double-side polished silicon wafer is given as 47.0 nm (flatness taken from [32]). Since we measure the step height of the Si wafer stack, the r.m.s. flatness is multiplied by $\sqrt{2}$, resulting in 66.5 nm uncertainty (Line 11). The thickness change due to thermal expansion (Line 12) of a 777 μm-thick Si wafer shows uncertainty of 0.042 nm ($= 2.6 \times 10^{-6} \times 0.021\ K \times 777000\ nm$). The thermal expansion coefficient at 298 K of the Si wafer is given as $2.6 \times 10^{-6} \cdot C^{-1}$ (coefficient taken from [34]) and the temperature variation during 0.5 ms averaging time on the Si wafer was measured to be 21 mK. When we include the uncertainty of the Si wafer, the combined uncertainty is 92.9 nm (Line c).

VI. Conclusion

We have demonstrated that the EOS-TD-based TOF detection with 785-nm femtosecond pulses is highly suitable for step height measurements and surface profilometry of Si-based devices. The EOS-TD-based surface imaging has the advantages of high precision as well as a large measurable range required in the 3D semiconductor inspection process. In particular, a light source with a center wavelength near the visible spectrum is suitable for precise imaging for semiconductor devices due to its shorter penetration depth in the silicon substrate. Since our method is also suitable for imaging the surface of various metallic surfaces as well as semiconductor materials, this can be applied for surface imaging of MEMS devices [35], skin-integrated sensors used in wearable devices [36], and biosensors [37].

We anticipate that the performance of the demonstrated TOF detection method at 785 nm can be further improved. For example, the use of higher microwave signal frequency, faster beam scanning with an acousto-optic deflector [38], and sharp-edged photocurrent pulses as a timing ruler signal [39] will improve the precision as well as measurement speed. Since the optical power loss in fiber optic devices is generally larger in the ~800 nm wavelength range compared to the telecommunication wavelength range, improving the optical power efficiency of the EOS-TDs may help to increase the detection sensitivity. We expect that an EOS-TD made with a dual-output Mach-Zehnder configuration [27], [28] might be also helpful due to its high sensitivities and potentially lower loss.

References

[1] S. Salahuddin, K. Ni, and S. Datta, “The era of hyper-scaling in electronics,” *Nature Electron.*, vol. 1, no. 8, pp. 442–450, Aug. 2018, doi: 10.1038/s41928-018-0117-x.

[2] D. Choudhury, “3D integration technologies for emerging microsystems,” in *Proc. IEEE MTT-S Int. Microw. Symp.*, May 2010, pp. 1–4.

[3] D. James, “3D ICs in the real world,” in *Proc. 25th Annu. SEMI Adv. Semicond. Manuf. Conf.*, May 2014, pp. 113–119.

[4] S. Jangam and S. S. Iyer, “Silicon-Interconnect fabric for fine-pitch (≤10 μm) heterogeneous integration,” *IEEE Trans. Compon. Packag. Manuf. Technol.*, vol. 11, no. 5, pp. 727–738, May 2021, doi: 10.1109/tcpmt.2021.3075219.

[5] M. Liebens et al., “Defect learning methodology applied to microbump process at 20 μm pitch and below,” in *Proc. 29th Annu. SEMI Adv. Semicond. Manuf. Conf.*, Apr. 2018, pp. 10–17.

[6] J. P. Gambino, S. A. Adderly, and J. U. Knickerbocker, “An overview of through-silicon-via technology and manufacturing challenges,” *Microelectron. Eng.*, vol. 135, pp. 73–106, Mar. 2015, doi: 10.1016/j.mee.2014.10.019.

[7] W. D. Van Driel, “Reliability consequences of the chip-package interactions,” in *Proc. 11th Electron. Packag. Technol. Conf.*, 2009, pp. 406–411.

[8] Y. Sawada, K. Harada, and H. Fujioka, “Study of package warp behavior for high-performance flip-chip BGA,” *Microelectron. Reliab.*, vol. 43, no. 3, pp. 465–471, Mar. 2003, doi: 10.1016/s0026-2714(02)00294-9.

[9] J. De Vos et al., “Key elements for sub-50μm pitch micro bump processes,” in *Proc. IEEE 63rd Electron. Compon. Technol. Conf.*, 2013, pp. 1122–1126.

[10] B. Dang et al., “Assembly, characterization, and reworkability of Pb-free ultra-fine pitch C4s for system-on-package,” in *Proc. Electron. Compon. Technol. Conf.*, 2007, pp. 42–48.

[11] N. G. Orji et al., “Metrology for the next generation of semiconductor devices,” *Nature Electron.*, vol. 1, pp. 532–547, Oct. 2018, doi: 10.1038/s41928-018-0150-9.

[12] A. G. Marrugo, F. Gao, and S. Zhang, "State-of-the-art active optical techniques for three-dimensional surface metrology: A review," *J. Opt. Soc. Amer. A*, vol. 37, no. 9, pp. B60–B77, Sep. 2020, doi: 10.1364/JOSAA.398644.

[13] B. Bunday et al., "The coming of age of tilt CD-SEM," in *Proc. Int. Soc. Opt. Eng.*, Apr. 2007, vol. 6518, Art. no. 65181S.

[14] K. Baek et al., "In situ TEM observation on the interface-type resistive switching by electrochemical redox reactions at a TiN/PCMO interface," *Nanoscale*, vol. 9, no. 2, pp. 582–593, Jan. 2017, doi: 10.1039/c6nr06293h.

[15] E. Solecky et al., "In-line E-beam metrology and defect inspection: Industry reflections, hybrid E-beam opportunities, recommendations and predictions," in *Proc. Metrology, Inspection, Process Control Microlithography XXXI (SPIE)*, Mar. 2017, vol. 10145, pp. 241–258.

[16] O. Custance, R. Perez, and S. Morita, "Atomic force microscopy as a tool for atom manipulation," *Nature Nanotechnol.*, vol. 4, no. 12, pp. 803–810, Dec. 2009, doi: 10.1038/nnano.2009.347.

[17] P. de Groot, "Principles of interference microscopy for the measurement of surface topography," *Adv. Opt. Photon.*, vol. 7, no. 1, pp. 1–65, Mar. 2015, doi: 10.1364/aop.7.000001.

[18] H. Ishigaki, I. Futamura, T. Okada, T. Mamiya, and Y. Hayasaki, "Height measurement of solder bumps using two-wavelength parallel four-step phase shifting digital holography," *Appl. Opt.*, vol. 60, no. 10, pp. B8–B13, Apr. 2021, doi: 10.1364/AO.414941.

[19] Y. Lu, J. Park, D. Bian, L. Yu, and S.-W. Kim, "Simultaneous 3-D surface profiling of multiple targets by repetition rate scanning of a single femtosecond laser," *Int. J. Precis. Eng. Manuf.*, vol. 21, no. 2, pp. 211–217, Feb. 2019, doi: 10.1007/s12541-019-00246-2.

[20] G. Xu, Y. Wang, S. Xiong, and G. Wu, "Digital-micromirror-device-based surface measurement using heterodyne interferometry with optical frequency comb," *Appl. Phys. Lett.*, vol. 118, no. 25, Jun. 2021, Art. no. 251104, doi: 10.1063/5.0050307.

[21] D. Semwogerere and E. R. Weeks, "Confocal microscopy," *Encyclopedia Biomaterials Biomed. Eng.*, vol. 23, pp. 1–10, 2005.

[22] K. Shibuya et al., "Scan-less hyperspectral dual-comb single-pixel-imaging in both amplitude and phase," *Opt. Exp.*, vol. 25, no. 18, pp. 21947–21957, Sep. 2017, doi: 10.1364/OE.25.021947.

[23] Y. Na et al., "Ultrafast, sub-nanometre-precision and multifunctional time-of-flight detection," *Nature Photon.*, vol. 14, no. 6, pp. 355–360, Jun. 2020, doi: 10.1038/s41566-020-0586-0.

[24] X. Lu et al., "Time-of-flight detection of femtosecond laser pulses for precise measurement of large microelectronic step height," *Opt. Lett.*, vol. 43, no. 7, pp. 1447–1450, Apr. 2018, doi: 10.1364/OL.43.001447.

[25] J. Kim, F. X. Kärtner, and M. H. Perrott, "Femtosecond synchronization of radio frequency signals with optical pulse trains," *Opt. Lett.*, vol. 29, pp. 2076–2078, Sep. 2004.

[26] C. Ahn, Y. Na, M. Hyun, J. Bae, and J. Kim, "Synchronization of an optical frequency comb and a microwave oscillator with 53 zs/Hz$^{1/2}$ resolution and 10^{-20}-level stability," *Photon. Res.*, vol. 10, no. 2, pp. 365–372, Feb. 2022, doi: 10.1364/prj.443316.

[27] M. Endo, T. D. Shoji, and T. R. Schibli, "High-sensitivity optical to microwave comparison with dual-output Mach-Zehnder modulators," *Sci. Rep.*, vol. 8, Mar. 2018, Art. no. 4388, doi: 10.1038/s41598-018-22621-1.

[28] A. H. Nejadmalayeri and F. X. Kärtner, "Mach-Zehnder based balanced optical microwave phase detector," in *Proc. Conf. Lasers Electro-Opt.*, May 2012, Art. no. CTu2A.1.

[29] M. Walbran, A. Gliserin, K. Jung, J. Kim, and P. Baum, "5-femtosecond laser-electron synchronization for pump-probe crystallography and diffraction," *Phys. Rev. Appl.*, vol. 4, no. 4, Oct. 2015, Art. no. 044013, doi: 10.1103/PhysRevApplied.4.044013.

[30] H. Yang et al., "10-fs-level synchronization of photocathode laser with RF-oscillator for ultrafast electron and X-ray sources," *Sci. Rep.*, vol. 7, Jan. 2017, Art. no. 39966, doi: 10.1038/srep39966.

[31] J. Shin et al., "Sub-10-fs timing for ultrafast electron diffraction with THz-driven streak camera," *Laser Photon. Rev.*, vol. 15, no. 2, Feb. 2020, Art. no. 2000326, doi: 10.1002/lpor.202000326.

[32] T. L. Schmitz, A. D. Davies, C. Evans, and R. E. Parks, "Silicon wafer thickness variation measurements using the National Institute of Standards and Technology infrared interferometer," *Opt. Eng.*, vol. 42, no. 8, pp. 2281–2290, Aug. 2003.

[33] J. Jin, Y. J. Kim, Y. Kim, S. W. Kim, and C. S. Kang, "Absolute length calibration of gauge blocks using optical comb of a femtosecond pulse laser," *Opt. Exp.*, vol. 14, no. 13, pp. 5968–5974, Jun. 2006.

[34] Y. Okada and Y. Tokumaru, "Precise determination of lattice parameter and thermal expansion coefficient of silicon between 300 and 1500 K," *J. Appl. Phys.*, vol. 56, no. 2, pp. 314–320, Jul. 1984.

[35] W. R. Ali and M. Prasad, "Piezoelectric MEMS based acoustic sensors: A review," *Sensors Actuators A: Phys.*, vol. 301, Jan. 2020, Art. no. 111756, doi: 10.1016/j.sna.2019.111756.

[36] D. Li, K. Yao, Z. Gao, Y. Liu, and X. Yu, "Recent progress of skin-integrated electronics for intelligent sensing," *Light: Adv. Manuf.*, vol. 2, no. 1, pp. 39–58, 2021, doi: 10.37188/lam.2021.004.

[37] A. Sheng et al., "Micro/nanodevices for assessment and treatment in stomatology and ophthalmology," *Microsyst. Nanoeng.*, vol. 7, pp. 1–19, Jan. 2021, doi: 10.1038/s41378-021-00238-1.

[38] A. C. Chan, E. Y. Lam, and K. K. Tsia, "Pixel super-resolution in optical time-stretch microscopy using acousto-optic deflector," in *Proc. Conf. Opt. Life Sci.*, Apr. 2015, Art. no. BW2A.7, doi: 10.1364/boda.2015.bw2a.7.

[39] M. Hyun, C. Ahn, Y. Na, H. Chung, and J. Kim, "Attosecond electronic timing with rising edges of photocurrent pulses," *Nature Commun.*, vol. 11, Jul. 2020, Art. no. 3667, doi: 10.1038/s41467-020-17460-6.